Electrochimica Acta 543 (2025) 147540

Contents lists available at ScienceDirect

Electrochimica Acta

journal homepage: www.journals.elsevier.com/electrochimica-acta

UV-polymerized composite ionogels for Li-organic batteries

Öykü Simsek [a,b,c,d], Mintao Wan [e,f], Philip Zimmer [a,b,c,d], Isaac Álvarez Moisés [g], Simon Muench [a,b], Jean-François Gohy [g], Dominic Bresser [e,f], Ulrich S. Schubert [a,b,c,d,*]

[a] Laboratory of Organic and Macromolecular Chemistry (IOMC), Friedrich Schiller University Jena, Humboldtstraße 10, 07743 Jena, Germany
[b] Center for Energy and Environmental Chemistry Jena (CEEC Jena), Friedrich Schiller University Jena, Philosophenweg 7a, 07743 Jena, Germany
[c] Helmholtz Institute for Polymers in Energy Applications Jena (HIPOLE Jena), Lessingstrasse 12-14, 07743 Jena, Germany
[d] Helmholtz-Zentrum Berlin für Materialen und Energie, 14109 Berlin, Germany
[e] Helmholtz Institute Ulm (HIU), Helmholtzstrasse 11, 89081, 89081 Ulm, Germany
[f] Karlsruhe Institute of Technology (KIT), P.O. Box 3640, 76021, Karlsruhe, Germany
[g] Institute of Condensed Matter and Nanosciences (IMCN), Université catholique de Louvain, Place Louis Pasteur 1, Louvain-la-Neuve, 1348, Belgium

ARTICLE INFO

Keywords:
Ionic liquid
Composite ionogel
Inorganic filler
Gel polymer electrolyte
UV-induced polymerization
Organic batteries
PTMA

ABSTRACT

In this work, we report novel ionogels produced *via* UV-induced free radical polymerization for lithium-organic cells. Before UV-polymerization for 75 min, the methacrylate- and methacrylamide-based monomers were mixed with a lithium salt-ionic liquid mixture and a photo-initiator. The thermal and electrochemical properties of these highly ionically conductive ionogels (0.9 mS cm^{-1} at 20 °C) were improved with the incorporation of Al_2O_3 particles. These composite ionogels show a significantly higher ionic conductivity (1.7 mS cm^{-1} at 20 °C) and much lower overpotential in addition to a thinner and more even SEI. Moreover, they increased the cycling performance when utilized as electrolyte and separator in Li//PTMA cells.

1. Introduction

Since their commercialization in the 1990s, lithium-ion batteries (LIBs) have been dominating the portable electronics market due to their high energy density (~500 Wh kg^{-1}) and good efficiency [1]. However, when higher energy densities or mechanical flexibility are required, this technology is limited. Additionally, they consist of toxic/scarce metals (e.g. nickel and cobalt) and flammable carbonate-based solvents, like ethylene carbonate (EC), diethyl carbonate (DEC), and dimethyl carbonate (DMC), which poses safety risks [2,3]. These liquid electrolytes (LEs) are not stable enough towards Li metal, dendrite growth may occur resulting in high resistance, short circuits, capacity decay, and thermal runaway coupled with possible side reactions between the LEs and Li metal causing the formation of an inhomogeneous solid electrolyte interphase (SEI) [4,5]. Furthermore, the Coulombic efficiency (CE) becomes lower owing to the continuous consumption of Li metal and the electrolyte, since the dendrite growth accelerates the SEI to be damaged and reformed again as cycling goes on [5]. Solid polymer electrolytes (SPEs) with their remarkable mechanical durability may block lithium dendrite growth, thus ensuring a long cycle life of lithium metal batteries (LMBs) [6]. Nonetheless, they suffer from low ionic conductivity at room temperature [7]. Gel polymer electrolytes (GPEs), a polymer matrix with immobilized LEs, overcome these drawbacks by combining the diffusive and cohesive properties of LEs and SPEs, respectively. Thus, they possess ionic conductivities around 1 mS cm^{-1} at ambient temperature, which allows them to be used for practical applications [8] act as separators [9] and reduce the leaking risk.

The LEs, which are embedded in the polymer structure to obtain the GPEs, can be divided into two categories: salts dissolved in low molar mass organic solvents and ionic liquid-based electrolytes (i.e., IL+ Li salt) [10]. Even though it is more common to use the former ones, their solvents are highly volatile, which brings on safety issues [10]. On the other side, ionic liquid-based GPEs, also referred to as ionogels (IGs), attracted great attention due to combining the safety of SPEs and the specific characteristics of ILs such as high ionic conductivity, broad electrochemical stability window (ESW), high thermal stability, nonvolatility, and nonflammability [11].

Recently, UV-induced photopolymerization has gained prominence as a method for ionogel preparation due to its distinct advantages, and it has also been adopted in our group's ongoing research efforts [12–15]. Firstly, the process facilitates a straightforward and cost-effective polymerization, thus obviating the necessity for complex synthesis

---

* Corresponding author.
E-mail address: ulrich.schubert@uni-jena.de (U.S. Schubert).

https://doi.org/10.1016/j.electacta.2025.147540
Received 22 April 2025; Received in revised form 26 September 2025; Accepted 7 October 2025

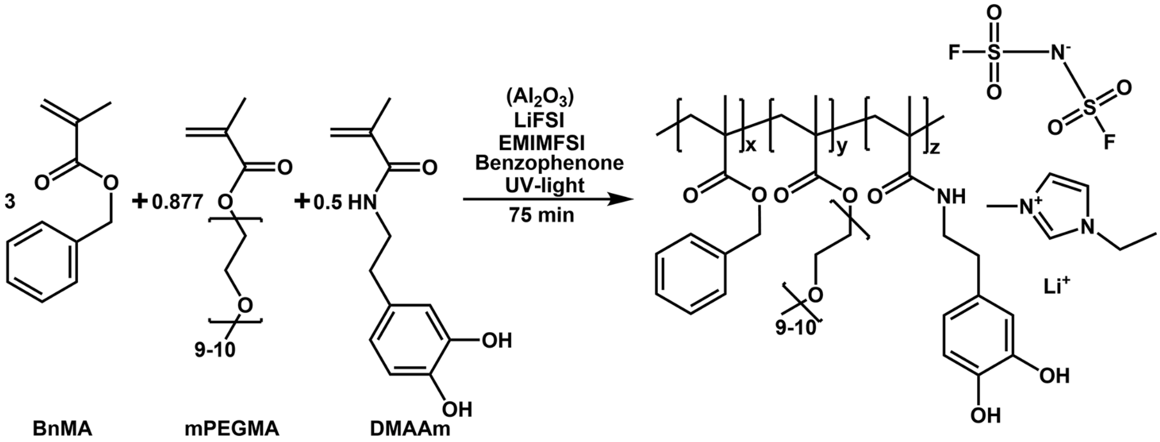

Scheme 1. Schematic representation of the synthesis of IG and CIG.

methods [16]. Secondly, the process can occur rapidly, even in seconds, depending on the photoinitiator used. Furthermore, the utilization of light facilitates temporal and spatial regulation of the curing process, given that polymerization transpires exclusively during the irradiation period (commencing at the onset of exposure and concluding upon its termination) and solely within irradiated domains [17]. Despite the plethora of studies conducted on UV-polymerized ionogels for battery applications, to the best of our knowledge, there has been no research undertaken on the types of PEs for Li-organic batteries presented in this work. Khatmullina et al. developed IGs composed of poly(ethylene glycol diacrylate) (PEGDA), lithium tetrafluoroborate ($LiBF_4$), 1-ethyl-3-methylimidazolium tetrafluoroborate ($EMIMBF_4$), and SiO_2 nanoparticles for Li-organic cells with the octalithium salt of octahydroxytetraazapentacene (LiOTAP, theoretical capacity of 468 mAh g^{-1}) as the cathode material [18]. Despite the dissolution issue of LiOTAP with the liquid electrolyte reported in the previous work [19] thanks to the use of IGs, this problem was not observed. Regarding the cell performance, a stable cycling behavior with a specific capacity of 150 mAh g^{-1} at 0.5C was obtained after a capacity loss in the first cycles. Kim et al. fabricated IGs by immersing nano-fibrous poly(vinylidene fluoride-*co*-hexafluoropropylene) (PVdF-HFP) in 1 M lithium bis(trifluoromethanesulfony)imide (LiTFSI) in *N*-butyl-*N*-methyl-pyrrolidinium bis(trifluoromethanesulfonyl)imide ($Pyr_{14}TFSI$) for Li//PTMA cells [20]. The cell with IG revealed a discharge capacity of 110 mAh g^{-1} at 1C and 33 mAh g^{-1} at 10C attributing a good rate capability.

Besides electrolytes, electrodes also play a key role in terms of electrochemical performance and safety. In the last years, organic cathodes gained a considerable interest due to the reversible and fast redox kinetics, being more environmentally friendly, displaying tunable properties, and low cost. They can be fabricated based on the stable organic radicals having unpaired electrons. 2,2,6,6-Tetramethylpiperidinyl-*N*-oxyl (TEMPO) is one of the commonly used stable organic radicals to prepare polymer-based cathodes. Poly(2,2,6,6-tetramethylpiperidinyl-*N*-oxy methacrylate) (PTMA), a polymer having TEMPO repeating units, has been reported by Nakahara et al. in 2002 and intensively studied [21].

In this work, we report a new UV-polymerized composite ionogel (CIG) exhibiting high ionic conductivity, a considerable anodic stability, high thermal stability, and good electrochemical performance. Further, the effect incorporating Al_2O_3 particles was investigated in terms of thermal and electrochemical properties. It was revealed that the addition of these particles results in an increased ionic conductivity, improved compatibility towards the Li anode, and stabilized galvanostatic cycling performance in Li//PTMA cells. These novel composite ionogels represent promising candidates for Li-organic batteries.

2. Experimental

1-Ethyl-3-methylimidazolium bis(fluorosulfonyl)imide (EMIMFSI, Proionic) and lithium bis(fluorosulfonyl)imide (LiFSI, Solvionic) were dried separately in a glass oven (Buchi oven B-585) at room temperature for 2 h, at 50 °C for 6 h, and at 80 °C for 12 h, first at 10^{-3} mbar and then with the same procedure at 10^{-7} mbar. Afterwards LiFSI and EMIMFSI were mixed in a molar ratio of 0.2 to 0.8 (hereinafter referred to as ILE). Subsequently, ILE was dried by using the same procedure mentioned above. All preparation and drying steps were carried out in a dry room (dew point < -70 °C). IGs and CIGs were fabricated *via* a one-pot UV-induced polymerization (main lines of 254, 313, 334, 365, 405, 436, 546, 578 nm, and a weak line near 690 nm by a mercury lamp, Dr. Hönle AG) with a final temperature of 54 °C in a dry room. Before use, the inhibitors of benzyl methacylate (BnMA) and poly(ethylene glycol) methyl ether methacrylate (mPEGMA, 500 g mol^{-1}) were removed by filtering through inhibitor remover (alumina particles) for hydroquinone and monomethyl ether hydroquinone (Sigma-Aldrich). For the preparation of the IGs, BnMA, mPEGMA, and dopamine methacrylamide (DMAAm) were mixed in a molar ratio of 3:0.877:0.5 and combined with ILE in a weight ratio of 30:70. Afterwards it was heated to 110 °C and 1.8 wt. % of benzophenone (photoinitiator) was added. For the CIGs, 5 % of positively charged Al_2O_3 particles (Aeroxide Alu 130, Evonik) were added to the monomer precursor having the same composition and then it was heated to 120 °C. The prepared mixtures were poured between two Mylar foils and UV-polymerized for 75 min. The obtained membranes were vacuum-dried at 80 °C overnight before usage. The overview of the reaction is shown in Scheme 1.

The synthesis of PTMA with multiwalled carbon nanotubes and the preparation of the eventual cathodes was reported and described in detail earlier [22,23]. Briefly, 2,2,6,6-tetramethyl-4-piperidyl methacrylate (TMPM 98 %, TCI) and azobis(isobutyronitrile) (AIBN, recrystallized in ethanol, TCI) were dissolved in acetone (VWR, technical grade), followed by the addition of ethylene glycol dimethacrylate (EGDME 98 %, Acros Organics) as a cross-linking agent. After solvent removal, the precursor mixture was ball-milled (Type S1, Retsch GmbH) with multi-walled carbon nanotubes (NC7000, Nanocyl), transferred to a glass reactor, and polymerized at 80 °C under argon overnight. The resulting polymer mixed with carbon was extracted, washed, dried, and ball-milled. To oxidize this intermediate product, the polymer-carbon mixture was dispersed in methanol (technical grade, VWR) and sodium tungstate (Na_2WO_4 99 %, Sigma-Aldrich), ethylenediaminetetraacetic sodium salt (EDTA 98.5 %, Sigma-Aldrich), and hydrogen peroxide (30 % H_2O_2, Sigma-Aldrich) were added. The reaction occurred at 60 °C for 48 h, followed by filtration, washing, drying, and ball milling to obtain the final product. The weight ratio between PTMA and multi-walled carbon nanotubes was 85:15.

2.1. Materials characterization

For the kinetics studies on the IGs, the precursor of the IG was UV-initiated for different polymerization times and the products were stirred in DMSO-d6 overnight. Thereafter, the obtained samples were filtered, and the remaining solutions were analyzed with ^{1}H NMR (Bruker AC 300 spectrometer). The EMIMFSI inside the gels was used as internal standard. ^{1}H NMR of the monomeric precursor of IG before photopolymerization (300 MHz, DMSO-d6, δ in ppm): 9.09 (EMIM CH); 8.76 (DMAAm OH); 8.65 (DMAAm OH); 7.91 (DMAAm NH); 7.74 (EMIM CH); 7.66 (EMIM CH); 7.30–7.41 (BnMA Ar); 6.40–6.68 (DMAAm Ar); 6.00–6.10 (mPEGMA+BnMA MA sp^2); 5.64–5.72 (mPEGMA+BnMA MA sp^2); 5.62 (DMAAm MAAm sp^2); 5.29 (DMAAm MAAm sp^2); 5.17 (BnMA Bn); 4.18 (EMIM CH$_2$); 3.84 (EMIM CH$_3$); 3.46–3.54 (mPEGMA EG); 3.18–3.28 (mPEGMA methoxy, DMAAm CH$_2$); 2.57 (DMAAm CH$_2$); 1.86–1.94 (mPEGMA+BnMA MA sp^3); 1.84 (DMAAm MAAm sp^3); 1.42 (EMIM CH$_3$).

Thermogravimetric analysis (TGA, Netzsch TG 209F1, under nitrogen atmosphere) was carried out by heating the overnight-dried samples from 25 to 600 °C with a heating rate of 10 K min^{-1}.

Non-isothermal experiments were carried out using a DSC 300 Caliris (Netzsch) under a nitrogen atmosphere (20 mL min^{-1}). The instrument was calibrated with indium and tin standards. Approximately ca. 5 mg of sample was measured. Data acquisition and evaluation were carried out using Proteus Analysis software. The samples were first heated from room temperature (RT = 25 °C) to 150 °C at a rate of 10 K min^{-1} and held for 3 min to erase the previous thermal history. Subsequently, they were cooled to −50 °C and heated again to 150 °C at a rate of 10 K min^{-1}.

Two-electrode pouch cells (ca. 2 cm^2) consisting of nickel foil as the working electrode and lithium foil as the counter electrode were built and linear sweep voltammetry (LSV) measurements (VMP Biologic potentiostat/galvanostat) were conducted in a voltage range from −0.2 to 5.5 V with a sweep rate of 1 mV s^{-1} at 20 °C for the determination of the electrochemical stability window of IG and CIG. Temperature dependent electrochemical impedance spectroscopy (EIS) was conducted in the frequency range from 1 MHz to 10 Hz with a voltage amplitude of 20 mV at temperatures from 0 to 50 °C applied to stainless steel/GPE/stainless steel two-electrode cells. The ionic conductivity of the IGs was determined with the software RelaxIS 3 (Version 3.0.22). Symmetric Li/(C)IG/Li cells were assembled for stripping-plating tests running at 0.01, 0.02, 0.05, and 0.1 mA cm^{-2} for 10 cycles, 2 h each, and long-term cycling at 0.02 mA cm^{-2} at 20 °C with a Maccor battery tester. The same system was used for galvanostatic cycling experiments. Li/IG-CIG/PTMA pouch cells were built in a dry room and cycled between 3.0 and 4.0 V for three cycles at 0.1C, five cycles each at 0.2C, 0.5C, 1C, and 2C, and finally at 1C. The temperature was set to 20 °C.

The compatibility of both IG and CIG with the Li electrode was investigated by *ex situ* scanning electron microscopy (SEM). After cycling, the Li/IG/PTMA and Li/CIG/PTMA cells were disassembled in a dry room. A Capella focused ion beam (FIB) with a gallium ion source, utilizing a milling current of 1.5 nA, was used to prepare the cross-sectional samples. To maintain sample integrity and prevent air contamination, all samples were transferred to the microscope under an argon atmosphere, facilitated by an air-tight transfer box (SEMILAB). Subsequently, the cross-sectional SEM analysis and energy dispersive X-ray (EDX) spectroscopy mapping were conducted using a ZEISS Crossbeam XB340 instrument equipped with an EDX spectrometer from X-treme Oxford Instruments.

3. Results and discussion

3.1. Synthesis and basic characterization

Kinetics studies were conducted to ascertain the optimal polymerization time, providing both high conversion and good film formation, using ^{1}H NMR spectroscopy. The double bond signals of the monomers (5.29 to 6.10 ppm) were used for the calculation of the monomer conversion. As seen in the spectra (**Fig. S1**), those signals became smaller assigning an increasing conversion. After 60 min, 90 % and 62 % conversion for methacrylate- and methacrylamide-based monomers, respectively, were obtained (**Fig. S2**). However, the film formation was not sufficient. Therefore, also a polymerization time of 75 min was tested and free-standing films were obtained, which can be ascribed to the much higher conversion values (i.e., 98 % for the methacrylate- and 83 % for the methacrylamide-based monomers) together with the continued crosslinking through the benzophenone. The benzophenone works as a dual-function photoinitiator and crosslinker forming the polymer network through a UV light-driven radical crosslinking process. Upon exposure to UV light, benzophenone is excited to its triplet state (BP*) making it a strong hydrogen atom abstractor. The benzophenone preferentially removes hydrogen atoms from polymer side chains, especially the phenolic –OH groups of dopamine methacrylamide (DMAAm) because the catechol groups in DMAAm have relatively weak O–H bonds, making them the primary sites for hydrogen abstraction and radical formation. These polymer macroradicals recombine, leading to the formation of covalent crosslinks between polymer chains. This process transforms the linear copolymer chains into a chemically crosslinked 3D polymer network. The formed random copolymer backbone bears side chains of mPEGMA, BnMA, and DMAAm. mPEGMA was chosen not only for its ether oxygen atoms, which coordinate Li$^+$ ions, allowing ion hopping or segmental motion–based conduction, but also for its contribution to the soft and flexible matrix, while BnMA provides mechanical strength, owing to π-π stacking of benzene rings. DMAAm is the comonomer mainly involved in crosslinking *via* radical-mediated coupling (semi-quinone coupling). Under UV exposure, catechol moieties can form semiquinone radicals. These radicals may then couple with one another, forming covalent C–C or C–O–C bonds and resulting in catechol–catechol dimers, which contributes to chemical crosslinking between polymer chains significantly [24]. Moreover, molecular dynamics simulations reported by Yeh et al. revealed strong catechol adsorption to alumina surfaces *via* hydrogen bonding [25]. Based on this findings, we hypothesize that such interactions in our system may contribute to improved cohesion and mechanical stability; however, experimental validation is required.

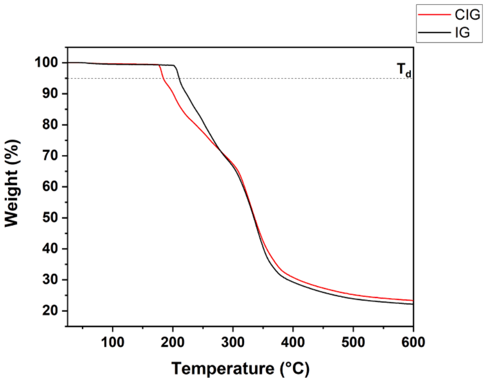

Fig. 1. Thermogravimetric analysis of IG and CIG.

Also, methacrylate-based monomers were found to demonstrate higher conversions than the methacrylamide-based ones for all polymerization times due to their higher reactivity. The free electron pair at the nitrogen in DMAAm leads to resonance stabilization and a more stable vinyl group [26,27]. In fact, according to Fugolin et al. [26] methacrylate-based monomers do not only react before methacrylamide-based ones, but also limit their reactivity when they are polymerized together.

In a next step, the IG and the composite containing also Al$_2$O$_3$ (CIG) were characterized regarding their thermal properties and amorphicity by thermogravimetric analysis (TGA) (Fig. 1) and differential scanning

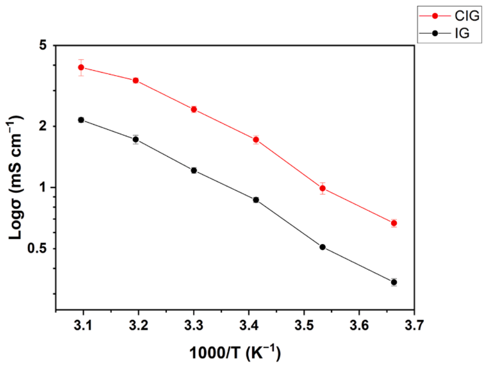

Fig. 2. Temperature dependence of the ionic conductivity of IG and CIG.

calorimetry (DSC) (**Fig. S3**). The temperatures of 5 % weight loss were taken as basis for the decomposition temperatures (T_d). Interestingly, IG was found to have a T_d of 211 °C, which is slightly higher than the T_d of CIG with 184 °C. Possibly, the catechol groups are binding to the Al_2O_3 particles and, therefore, the number of catechol groups, which provide hydrogen bonds that are increasing the thermal stability, decreases, which may affect the TGA curve. Nevertheless, both electrolytes have good thermal stabilities. DSC analysis of the IG and CIG revealed no discernible thermal transitions such as a glass transition (T_g) or melting points within the measured temperature range (−50 to 120 °C), indicating that both materials are predominantly amorphous. The absence of a T_g suggests high segmental mobility likely due to the plasticizing effect of the IL and the mPEGMA comonomer.

3.2. Electrochemical characterization

Following the kinetics and thermal characterization, the electrochemical characterization was performed, starting with the determination of the ionic conductivity as a function of temperature (Fig. 2). Generally, the conductivity is increasing with increasing temperatures owing to the greater segmental dynamics, and higher for CIG than for IG. At 0 °C, for instance, the conductivity was 0.3 and 0.7 mS cm^{-1} for IG and CIG, respectively, which increased to 0.5 mS cm^{-1} in the case of IG at 10 °C, while it increased to 1 mS cm^{-1} in the case of CIG, which is considered suitable for practical applications [28]. At 20 °C, IG exhibited an ionic conductivity of 0.9 mS cm^{-1}, while CIG showed an ionic conductivity of 1.7 mS cm^{-1}, i.e., about twice as high. This factor of about two was maintained across the whole temperature range studied herein, in fact, indicating that the presence of the Al_2O_3 particles has sustainably positive effect on the ionic conductivity of these electrolytes which is hypothesized to be the result of two possible factors. As indicated by extant literature, catechol groups have been observed to coordinate with Li^+ ions [29–31] a process which may potentially impede the transport of ions. In the case of CIG, it is conceivable that those

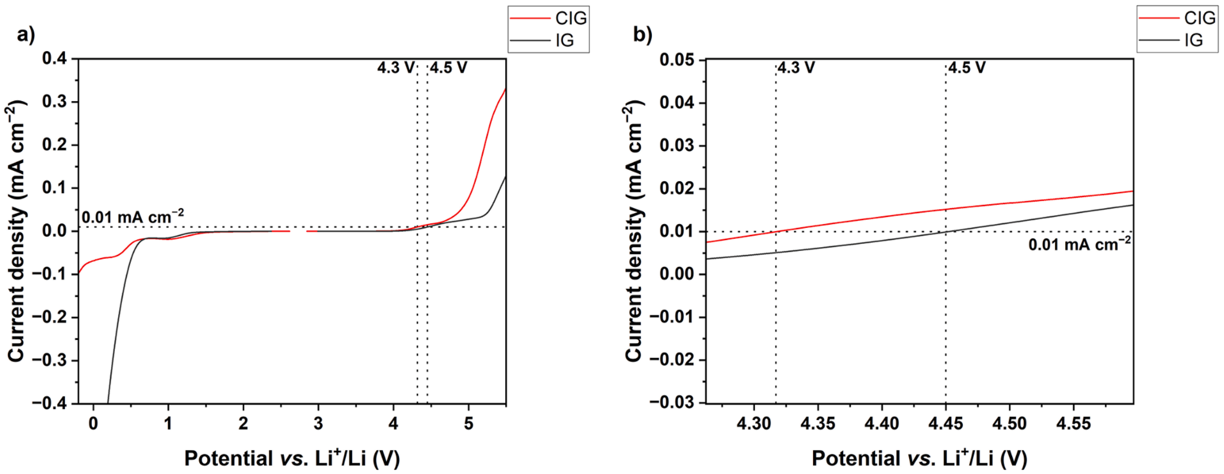

Fig. 3. (a) Determination of the ESW of IG and CIG *via* LSV. (b) Magnification of the area around the dashed lines in panel (a).

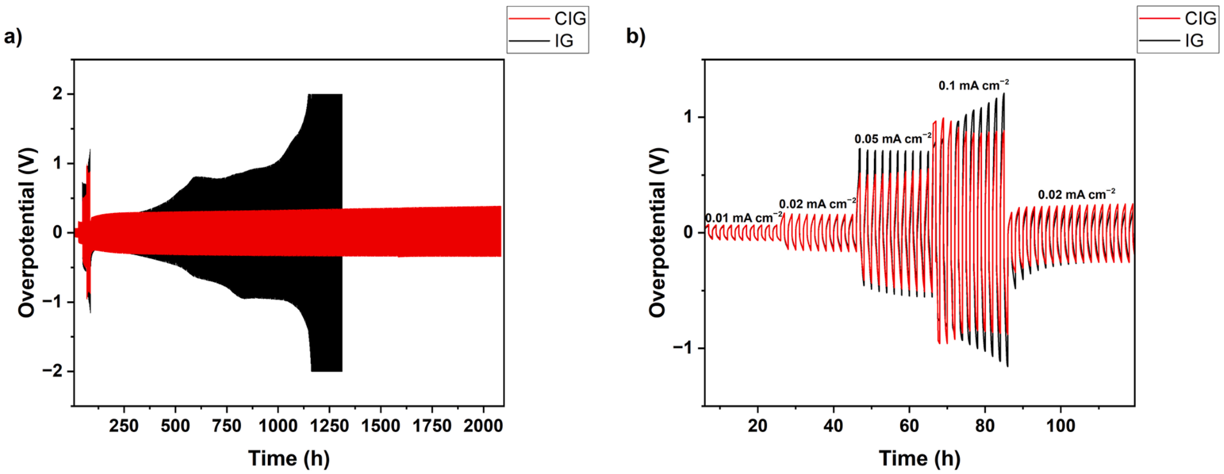

Fig. 4. Time-overpotential profiles of IG and CIG during Li stripping and plating at 0.01, 0.02, 0.05, 0.1, and 0.02 mA cm^{-2}: (a) plot of the complete experiment for >2000 h; (b) plot of the first 105 h (T = 20 °C).

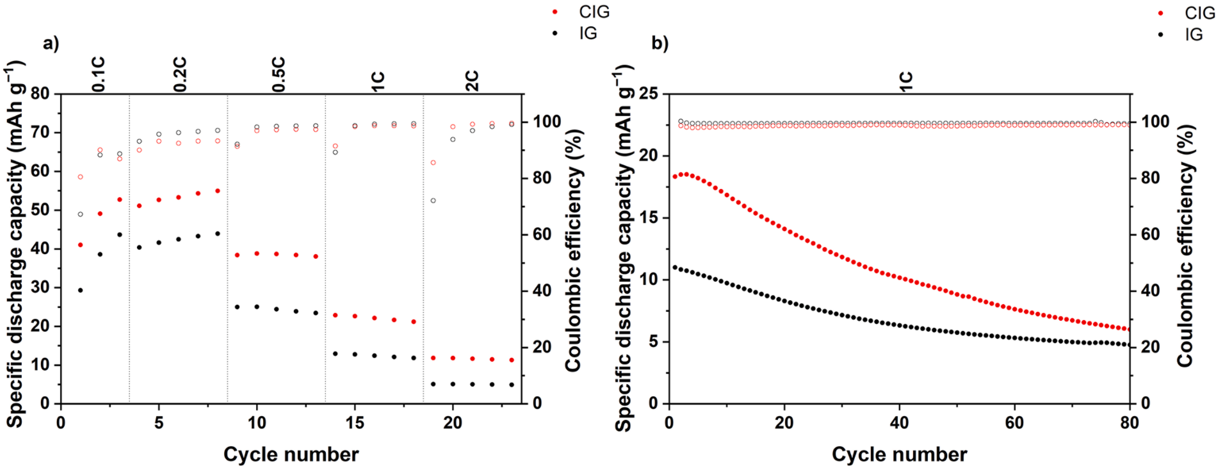

Fig. 5. Galvanostatic cycling of Li/IG/PTMA and Li/CIG/PTMA cells at (a) varying C rates from 0.1C to 2C, and (b) a constant C rate of 1C (cut-off voltages: 3.0 and 4.0 V vs. Li^+/Li; $T = 20$ °C).

groups interact with Al_2O_3 particles *via* hydrogen bonding [25] possibly increasing the mobility of Li^+ ions, thereby enhancing the ionic conductivity. Moreover, due to the positive charge of these particles, there is a possibility for interaction with FSI^- anions, facilitating ion transport [3].

Subsequently, the ESW was determined *via* LSV (Fig. 3). Generally, IG and CIG are characterized by a rather similar behavior – as expected from the fact that the only difference is the presence of the alumina in CIG (Fig. 3**a**). There are some minor differences, though. The processes observed around 0.98 V for IG and 1.01 V for CIG can be attributed to the reduction of $EMIM^+$ cation [32]. While Li^+ plating was expected to occur near 0 V, a shift in electrochemical activity was observed around 0.75 V for IG, in contrast to CIG, where the response remained at 0 V. The cathodic scan was difficult to interpret, which is consistent with previous reports where the anodic scan of the LE containing the same Li salt and IL also remained unresolved [33]. Previously, the oxidative stability

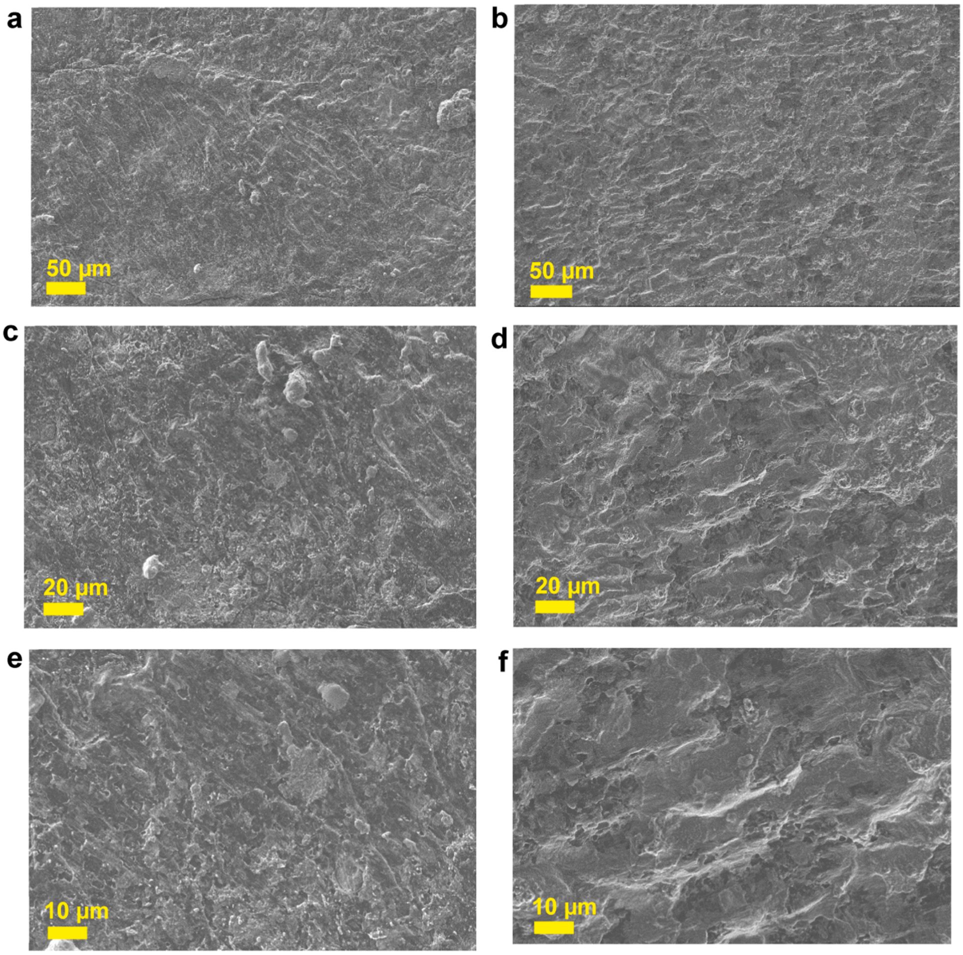

Fig. 6. SEM micrographs of the lithium-metal anodes after cycling using (a-c-e) IG or (b-d-f) CIG as the electrolyte in Li//PTMA cells.

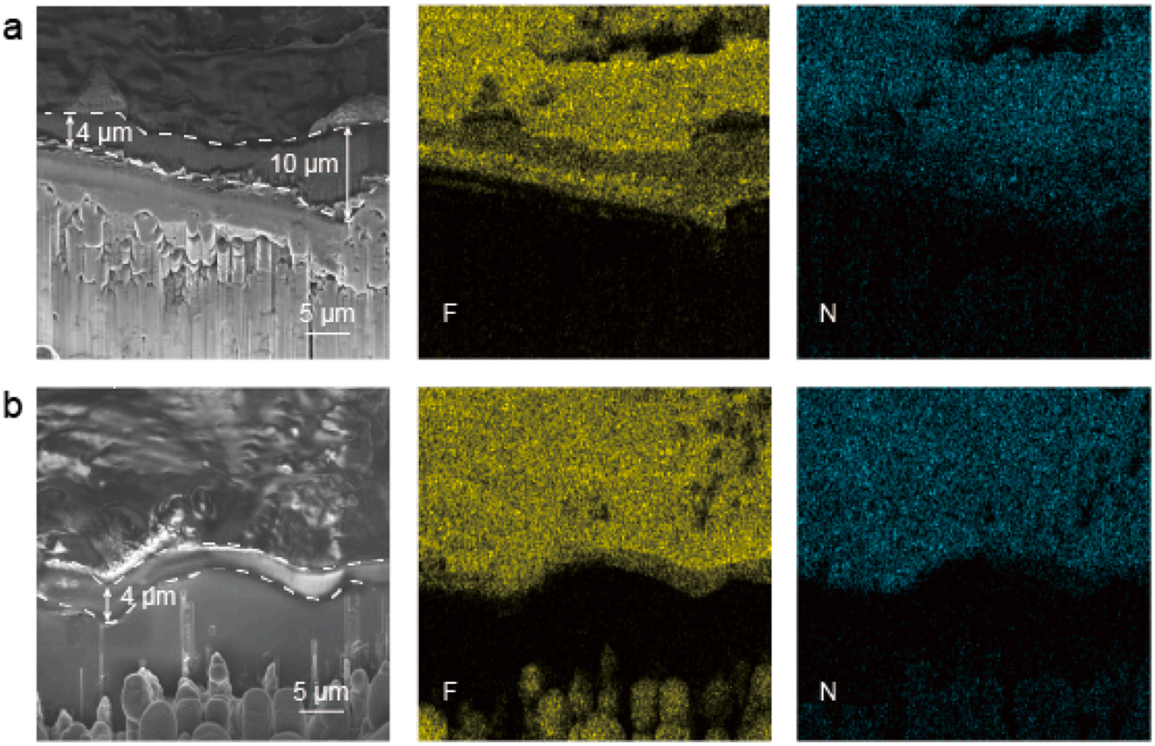

Fig. 7. Cross-sectional SEM micrographs of the lithium-metal anodes and the corresponding EDX mapping of F and N after cycling using (a) IG and (b) CIG.

threshold was expressed as 0.01 mA cm^{-2} by Dong et al. [34] According to this threshold, IG and CIG start to decompose at 4.5 V and 4.3 V, respectively, upon oxidation. While this relatively large gap is based on rather small difference (Fig. 3**b**), the sharp upturn in current occurs significantly earlier for CIG, which might be related to a difference in conductivity, as the alumina is supposed to be stable towards further oxidation. Nonetheless, both electrolytes are sufficiently stable for the targeted voltage window, which is between 3.0 and 4.0 V for PTMA.

For a better understanding of the stability of the electrolytes towards Li metal, Li stripping and plating tests were carried out, using symmetric Li/(C)IG/Li cells and setting the current density to 0.01, 0.02, 0.05, 0.1, and again to 0.02 mA cm^{-2} at 20 °C (Fig. 4). Although IG and CIG showed similar overpotentials of 67 vs. 68 mV and 148 vs. 160 mV at the end of the stripping/plating cycles at 0.01 and 0.02 mA cm^{-2}, respectively, the difference increased. At further elevated current densities, e. g., at 0.05 mA cm^{-2}, this difference in overpotential remained with, for instance, about 716 mV for IG and ca. 503 mV for CIG. In fact, when further increasing the current density to 0.1 mA cm^{-2}, the overpotential increased to >1 V for IG, while it remained stable well below 1 V for CIG. This improved cycling behavior by CIG can be explained with the addition of Al_2O_3 particles diminishing the overpotential and blocking the dendrite growth formation due to the strong affinity with the lithium metal anode as suggested by Cui et al. [35] Generally, in any case, no short-circuiting was observed for the two systems. Nonetheless, owing to the lower overpotential and higher ionic conductivity, CIG appears favorable for practical applications compared to IG.

The beneficial properties of CIG compared to IG were further corroborated by conducting galvanostatic cycling experiments on Li/(C) IG/PTMA at varying C rates (Fig. 5). After initial specific discharge capacities of ca. 30 and 40 mAh g^{-1} in the first cycle, delivered by the cells containing IG and CIG, respectively, at 0.1C, the cells showed reversible specific capacities of ca. 44 and 55 mAh g^{-1} at 0.2C. At 1C, the capacity decreased to around 12 and 21 mAh g^{-1} for IG and CIG, respectively, and at 2C to about 5 and 12 mAh g^{-1}. At higher C-rates (data not shown here), no significant capacity was observed. When getting back to 1C, the specific capacity recovered to ca. 11 mAh g^{-1} for IG and ca. 18 mAh g^{-1} for CIG, i.e., values that are fairly close to the earlier ones obtained at this C-rate. Nevertheless, both kinds of cells revealed a continuous fading upon the subsequent 1C cycling, indicating that there is presumably a need to further enhance the stability towards metallic lithium, e.g., by optimizing the polymerization reaction and reducing the amount of remaining monomers to essentially zero, while the incorporation of Al_2O_3 appears generally favorable.

3.3. *Ex situ SEM/EDX characterization of cycled lithium-metal anodes*

Ex situ SEM was performed to investigate the effect of the two different electrolyte systems on the repeated lithium stripping and plating. Fig. 6 presents the SEM micrographs of the Li electrodes from cells containing IG (Fig. 6**a**) and CIG (Fig. 6**b**) as the electrolyte. While the appearance is generally very similar, there are some particle-like deposits observed in the case of IG, potentially indicating an increased reactivity at the electrode|electrolyte interface and a less homogeneous lithium deposition. Differently, there are no such particle-like features observed in Fig. 6**b**, indicating a more homogeneous lithium plating and stripping for CIG.

Cross-sectional SEM micrographs of the cycled lithium-metal electrodes using IG as the electrolyte (**Fig. S4**), along with the corresponding EDX mapping of F and N (originating from the IL), reveal an uneven SEI thickness ranging from 4 to 10 μm (Fig. 7**a**). Additionally, a porous lithium deposition structure was found beneath the uneven SEI. In contrast, the SEI formed on the lithium using CIG as electrolyte is more uniform, with a consistent thickness of about 4 μm (Fig. 7**b**). Moreover, the cross-section micrographs show that the lithium deposition on the lithium-metal electrode cycled with the CIG electrolyte is denser. This difference can be ascribed to the Al_2O_3 particles contributing to a more stable SEI and engrossing the impurities which brings out a thinner SEI [36,37]. This more even and thinner SEI promotes a more homogeneous lithium stripping/plating process, resulting in better cycling stability for the cell using the CIG electrolyte.

4. Conclusion

IGs composed of a methacrylate- and methacrylamide-based polymer network, EMIMFSI, and LiFSI, were synthesized *via* solvent-free photopolymerization. In order to improve the electrochemical and morphological properties, composite IGs with Al_2O_3 particles (CIGs) were also prepared and the comparative results were given. The integration of Al_2O_3 particles enhanced the ionic conductivity (0.9 vs. 1.7 mS cm^{-1} at 20 °C), lowered the overpotential (716 mV vs. 503 mV at 0.05 mA cm^{-2}) together with more stable cycling behavior, and increased the delivered capacity significantly (12 vs. 21 mAh g^{-1} at 1C). Besides, SEM and FIB results confirmed that CIGs demonstrated a more homogeneous Li surface in addition to a thinner and more even SEI contributing to a better cell performance.

CRediT authorship contribution statement

Öykü Simsek: Writing – original draft, Visualization, Validation, Methodology, Investigation, Formal analysis, Data curation, Conceptualization. **Mintao Wan:** Writing – review & editing, Investigation, Formal analysis, Data curation. **Philip Zimmer:** Writing – review & editing, Formal analysis. **Isaac Álvarez Moisés:** Resources. **Simon Muench:** Writing – review & editing, Supervision. **Jean-François Gohy:** Writing – review & editing, Supervision. **Dominic Bresser:** Writing – review & editing, Supervision. **Ulrich S. Schubert:** Writing – review & editing, Supervision, Resources.

Declaration of competing interest

The authors declare the following financial interests/personal relationships which may be considered as potential competing interests:

Ulrich S. Schubert reports financial support was provided by European Union. If there are other authors, they declare that they have no known competing financial interests or personal relationships that could have appeared to influence the work reported in this paper.

Acknowledgement

The authors would like to acknowledge the financial support from the European Union's Horizon 2020 research and innovation program under the Marie Skłodowska-Curie grant agreement No 860403. The authors furthermore thank Dr. Alessandro Innocenti for the cathodes preparation, Dr. Matteo Gandolfo for the fruitful discussions, and Dr. Valentina Pirela Wilhelm for DSC measurements.

Supplementary materials

Supplementary material associated with this article can be found, in the online version, at doi:10.1016/j.electacta.2025.147540.

Data availability

Data will be made available on request.

References

[1] T. Placke, R. Kloepsch, S. Dühnen, M. Winter, J. Solid State Electrochem. 21 (2017) 1939–1964.
[2] F. Mueller, N. Loeffler, G.T. Kim, T. Diemant, R.J. Behm, S. Passerini, ChemSusChem 9 (2016) 1290–1298.
[3] M. Gandolfo, D. Versaci, C. Francia, S. Bodoardo, J. Amici, Electrochim. Acta 463 (2023) 142857.
[4] R. Bhattacharyya, B. Key, H. Chen, A.S. Best, A.F. Hollenkamp, C.P. Grey, Nat. Mater. 9 (2010) 504–510.
[5] S. Fang, Y. Zhang, X. Liu, Chem. Eng. J. 426 (2021) 131880.
[6] C. Han, X. Shui, G. Chen, G. Xu, J. Ma, S. Dong, S. Wang, X. Zhou, Z. Cui, L. Qiao, Giant (2024) 100337.
[7] P. Isken, M. Winter, S. Passerini, A. Lex-Balducci, J. Power Sources 225 (2013) 157–162.
[8] K. Xu, Chem. Rev. 104 (2004) 4303–4418.
[9] M.S. Ahmed, M. Islam, B. Raut, S. Yun, H.Y. Kim, K.-W. Nam, Gels 10 (2024) 563.
[10] J. Castillo, A. Santiago, X. Judez, I. Garbayo, J.A. Coca Clemente, M.C. Morant-Miñana, A. Villaverde, J.A. González-Marcos, H. Zhang, M. Armand, Chem. Mater. 33 (2021) 8812–8821.
[11] J. Tang, B. Zhai, J. Liu, W. Ren, Y. Han, H. Yang, Y. Chen, C. Zhao, Y. Fang, Phy. Chem. Chem. Phys. 23 (2021) 6775–6782.
[12] S. Muench, R. Burges, A. Lex-Balducci, J.C. Brendel, M. Jäger, C. Friebe, A. Wild, U. S. Schubert, Energy Storage Mater. 25 (2020) 750–755.
[13] L. Elbinger, E. Schröter, P. Zimmer, C. Friebe, M. Osenberg, I. Manke, U. S. Schubert, J. Phys. Chem. C 128 (2024) 11465–11476.
[14] Ö. Simsek, P. Zimmer, S. Muench, U.S. Schubert, J. Power Sources Adv. 33 (2025) 100176.
[15] Ö. Simsek, A. Innocenti, I.Á. Moisés, P. Zimmer, Z. Lyu, S. Muench, J.-F. Gohy, D. Bresser, U.S. Schubert, J. Power Sources Adv. 35 (2025) 100186.
[16] I. Cárdaba, L. Porcarelli, A. Gallastegui, D. Mecerreyes, M.I. Maguregui, Polymers 13 (2021) 2108.
[17] E. Andrzejewska, Polym. Int. 66 (2017) 366–381.
[18] K.G. Khatmullina, N.A. Slesarenko, A.V. Chernyak, G.R. Baymuratova, A. V. Yudina, M.P. Berezin, G.Z. Tulibaeva, A.A. Slesarenko, A.F. Shestakov, O. V. Yarmolenko, Membranes 13 (2023) 548.
[19] A. Slesarenko, I.K. Yakuschenko, V. Ramezankhani, V. Sivasankaran, O. Romanyuk, A.V. Mumyatov, I. Zhidkov, S. Tsarev, E.Z. Kurmaev, A. F. Shestakov, J. Power Sources 435 (2019) 226724.
[20] J.-K. Kim, A. Matic, J.-H. Ahn, P. Jacobsson, RSC Adv. 2 (2012) 9795–9797.
[21] K. Nakahara, S. Iwasa, M. Satoh, Y. Morioka, J. Iriyama, M. Suguro, E. Hasegawa, Chem. Phys. Lett. 359 (2002) 351–354.
[22] A. Vlad, J. Rolland, G. Hauffman, B. Ernould, J.F. Gohy, ChemSusChem 8 (2015) 1692–1696.
[23] A. Innocenti, I.Á. Moisés, O. Lužanin, J. Bitenc, J.-F. Gohy, S. Passerini, ACS Appl. Mater. Interfaces. 16 (2023) 48757–48770.
[24] J. Yang, M.A.C. Stuart, M. Kamperman, Chem. Soc. Rev. 43 (2014) 8271–8298.
[25] I.-C. Yeh, J.L. Lenhart, B.C. Rinderspacher, J. Phys. Chem. C 119 (2015) 7721–7731.
[26] A.P. Fugolin, S. Lewis, M.G. Logan, J.L. Ferracane, C.S. Pfeifer, Dent. Mater. 36 (2020) 1028–1037.
[27] L. Barcelos, M. Borges, C. Soares, M. Menezes, V. Huynh, M. Logan, A. Fugolin, C. Pfeifer, Dent. Mater. 36 (2020) 468–477.
[28] M. Joost, M. Kunze, S. Jeong, M. Schönhoff, M. Winter, S. Passerini, Electrochim. Acta 86 (2012) 330–338.
[29] B.J. Sandmann, H.T. Luk, J. Pharm. Sci. 75 (1986) 73–77.
[30] N. Patil, A. Mavrandonakis, C. Jérôme, C. Detrembleur, J. Palma, R. Marcilla, ACS Appl. Energy Mat. 2 (2019) 3035–3041.
[31] N. Patil, A. Mavrandonakis, C. Jérôme, C. Detrembleur, N. Casado, D. Mecerreyes, J. Palma, R. Marcilla, J. Mater. Chem. A 9 (2021) 505–514.
[32] C.J. Jafta, X.G. Sun, H. Lyu, H. Chen, B.P. Thapaliya, W.T. Heller, M.J. Cuneo, R. T. Mayes, M.P. Paranthaman, S. Dai, Adv. Funct. Mater. 31 (2021) 2008708.
[33] X. Liu, T. Diemant, A. Mariani, X. Dong, M.E. Di Pietro, A. Mele, S. Passerini, Adv. Mater. 34 (2022) 2207155.
[34] X. Dong, A. Mayer, X. Liu, S. Passerini, D. Bresser, ACS Energy Lett. 8 (2023) 1114–1121.
[35] S. Cui, X. Wu, Y. Yang, M. Fei, S. Liu, G. Li, X.-P. Gao, ACS Energy Lett. 7 (2021) 42–52.
[36] G. Appetecchi, F. Croce, L. Persi, F. Ronci, B. Scrosati, Electrochim. Acta 45 (2000) 1481–1490.
[37] E. Peled, D. Golodnitsky, G. Ardel, V. Eshkenazy, Electrochim. Acta 40 (1995) 2197–2204.